

EFFICIENT GEOSYNCHRONOUS CIRCULAR SAR RAW DATA SIMULATION OF EXTENDED 3-D SCENES

Q. Liu^{1,2,3,*}, W. Hong^{1,2}, W.-X. Tan^{1,2}, and Y.-R. Wu^{1,2}

¹National Key Laboratory of Science and Technology on Microwave Imaging Laboratory, No. 19, BeiSiHuan XiLu, Beijing, China

²Institute of Electronics, Chinese Academy of Sciences, No. 19, BeiSiHuan XiLu, Beijing, China

³Graduate University of Chinese Academy of Sciences, No. 19A, YuQuanLu, Beijing, China

Abstract—Geosynchronous Circular Synthetic Aperture Radar (GeoCSAR) has the Circular SAR configuration and undergoes a near-ellipse geosynchronous track rather a “8”-like track of conventional GeoSAR. It could produce three dimensional (3-D) images of extended Earth scenes. GeoCSAR raw data simulator is of vital for predicting system performance, developing suitable data processing algorithms, etc.. It should include degrading conditions such as motion instability, angular deviations and orbit perturbations in order to approach the real situation. The common generation algorithm of raw data in time domain is precise but time-consuming for extended 3-D scene. In this paper, a novel raw data simulation algorithm based on inverse Improved Polar Format Algorithm (IPFA) for GeoCSAR was proposed, which possessed both the advantages of precision of time domain simulator and efficiency of frequency domain simulator. Implementation details were presented, and several simulation results were provided and analyzed to validate the algorithm.

1. INTRODUCTION

Geosynchronous Synthetic Aperture Radar (GeoSAR) has received more and more attention since it possesses many advantages compared to the low-Earth orbit SAR. Conventional GeoSAR usually undergoes a “8”-like track, and the whole track is not fully utilized [1, 2].

Received 3 March 2012, Accepted 17 April 2012, Scheduled 20 April 2012

* Corresponding author: Qi Liu (cadyfire@163.com).

Geosynchronous Circular Synthetic Aperture Radar (GeoCSAR) is a novel Circular SAR configuration which undergoes a near-ellipse geosynchronous track relative to the illuminated area [3]. It can achieve additional benefits like 3-D imaging, continuous monitoring, large size of antenna-beam footprint, etc.. SAR raw data simulator for GeoCSAR is particularly useful for software architecture and imaging algorithm designing, system verification and mission planning.

GeoCSAR raw data simulation is faced with several problems: (1) The synthetic aperture of GeoCSAR is a near-ellipse track which could not be approximated by lines or a perfect circle; (2) The factor of perturbations makes the real track far from being ideal [3]; (3) Due to the long slant range, the illumination area is very large and could not be regarded as a flat plain.

Time-domain simulator could generate raw data precisely via calculating and adding the reflected pulse from each point scatterer for all sensor trajectory positions. However, this approach is restricted to a scene composed of a limited number of discrete scatterers on a nonbackscattering background for its computational inefficiency [4–7]. Efficient raw data simulators for extended scenes operating in the frequency domain are discussed in [8–10]. However, these methods concentrate on the traditional linear aperture and thus cannot be applied to the two dimensional irregular apertures. Besides, the existing frequency-domain imaging methods based on wavefront reconstruction theory for Circular SAR [11–13] could only be applied to ideal circular geometry without any arbitrary deviation. Thus, the corresponding inverse process could not be used for GeoCSAR raw data simulation.

In this paper, an efficient frequency-domain raw data simulator based on an inverse improved PFA algorithm [3] for GeoCSAR is proposed. The Projection Slice Theorem (PST) is firstly applied in the simulation procedure with the assumption of planar wavefronts around a central reference point. Then, the conversion of planar wavefronts to spherical wavefronts is realized by a 1-D resampling operation so that the size of simulated scene is no longer limited by the range curvature phase error. The operation enables the simulator to use Fast Fourier transform (FFT) in the first step and generates raw data for non-ideal sensor trajectories precisely in the second step.

Section 2 presents the GeoCSAR signal model in both time and frequency domain. Section 3 describes the GeoCSAR simulation algorithm in detail. Section 4 exhibits the simulating results to verify the algorithm.

2. GEOCSAR SIGNAL MODEL

Figure 1 shows GeoCSAR imaging geometry in Earth-rotating coordinate system. The Y - Z plane is equatorial plane of Earth. Let satellite position vector be $\mathbf{r}_S = (r_S, \alpha_S, \theta_S)$ and target position be $\mathbf{r}_T = (r_T, \alpha_T, \theta_T)$ in spherical coordinates. The effect of orbital perturbations and stationkeeping on geosynchronous orbit has been discussed in [3].

Assume that the transmitted signal is a chirp with the following form:

$$p(t) = \text{rect}(t/T) \exp(-j\pi b_r t^2) \tag{1}$$

where t is the fast time, T is the pulse duration, b_r is the chirp rate, and B is the bandwidth of the chirp. The raw data of the scene can be described as:

$$s(\rho, \mathbf{r}_S) = \int_V \sigma(\mathbf{r}_T) G_a(\mathbf{r}_S, \mathbf{r}_T) p(\rho - |\mathbf{r}_S - \mathbf{r}_T|) \times \exp\left\{-j\frac{4\pi}{\lambda} |\mathbf{r}_S - \mathbf{r}_T|\right\} d\mathbf{r}_T \tag{2}$$

where $\sigma(\mathbf{r}_T)$ is the terrain reflectivity at (x_T, y_T, z_T) in Cartesian coordinates, c is the speed of light, $G_a(\mathbf{r}_S, \mathbf{r}_T)$ is the antenna beam pattern, $\rho = t \cdot c/2$ is range spatial domain, λ and f_c are carrier wavelength and frequency of the transmitted signal, respectively.

Assume that the scene is illuminated by the main antenna beam at all times, so $G_a(\mathbf{r}_S, \mathbf{r}_T)$ is neglected thereafter. Targets are illuminated in all orientations so that all targets are assumed to be isotropic, which is different from linear SAR [14, 15]. Via range

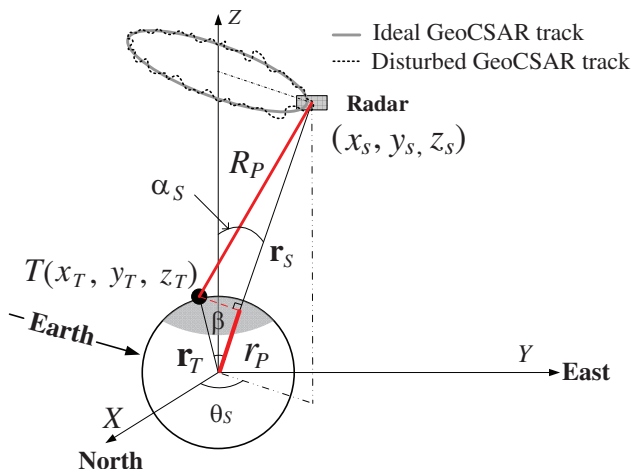


Figure 1. Imaging geometry of GeoCSAR.

FFT, the SAR raw data in range frequency domain (i.e., wavenumber domain) is [9]

$$\begin{aligned} s(k, \mathbf{r}_S) &= \frac{f_s}{\sqrt{|b_r|}} \text{rect} \left(\frac{f}{B} \right) \exp\{j\pi/4\} \exp\{-j\pi f^2/b_r\} \\ &\quad \times \iiint \sigma(x_T, y_T, z_T) g_{\mathbf{r}_S}(f, x_T, y_T, z_T) dx_T dy_T dz_T \\ &= \frac{f_s}{\sqrt{|b_r|}} \exp\{j\pi/4\} \exp\{-j\pi f^2/b_r\} \cdot E(k, \mathbf{r}_S) \end{aligned} \quad (3)$$

where $k = 4\pi f/c$ is the wavenumber, and f is the temporal frequency. $E(k, \mathbf{r}_S)$ is the signal after range compression, i.e.,

$$E(\rho, \mathbf{r}_S) = \iiint \sigma(x_T, y_T, z_T) \left(\frac{2B}{c}(\rho - R_P) \right) dx_T dy_T dz_T \quad (4)$$

$g_{\mathbf{r}_S}(f, x_T, y_T, z_T)$ is the SAR imaging system's shift-varying impulse response function:

$$g_{\mathbf{r}_S}(f, x_T, y_T, z_T) = \exp\{j\Phi\} = \exp(-jk \cdot R_P) \quad (5)$$

R_P is the range from satellite to target T , i.e.,

$$\begin{aligned} R_P &= |\mathbf{r}_S - \mathbf{r}_T| = \sqrt{(x_S - x_T)^2 + (y_S - y_T)^2 + (z_S - z_T)^2} \\ &= \sqrt{r_S^2 + r_T^2 - 2r_S r_T \cos \beta} \end{aligned} \quad (6)$$

where β is the angle between position vectors \mathbf{r}_S and \mathbf{r}_T

$$\cos \beta = \sin \alpha_S \sin \alpha_T \cos(\theta_S - \theta_T) + \cos \alpha_S \cos \alpha_T \quad (7)$$

The efficient GeoCSAR raw data simulator operates in the spatial frequency domain. However, the signal is collected in polar format (the slow time is the aspect angle θ_S), so that FFT cannot be applied directly. To accomplish this transform, the instantaneous wavenumber with respect to x , y , z direction is obtained through the first partial derivatives of Φ :

$$\begin{cases} k_x = \frac{\partial \Phi}{\partial x_S} = -k \frac{x_S - x_T}{R_P} \\ k_y = \frac{\partial \Phi}{\partial y_S} = -k \frac{y_S - y_T}{R_P} \\ k_z = \frac{\partial \Phi}{\partial z_S} = -k \frac{z_S - z_T}{R_P} \end{cases} \quad (8)$$

From Equation (5) and Equation (6), the GeoCSAR system transfer function $g_{\mathbf{r}_S}$ depends on the 3-D coordinate of ground point,

so does the corresponding frequency support $\psi(k_x, k_y, k_z)$ which can be achieved through Equation (8).

As shown in Figure 2(a), the data surface observed in the spatial frequency space is approximately a leaning truncated cone. The leaning angle and shape are both spatially variant. Thus, the point spread functions (PSF) and the resolutions in the focused GeoCSAR 3-D image are spatially variant.

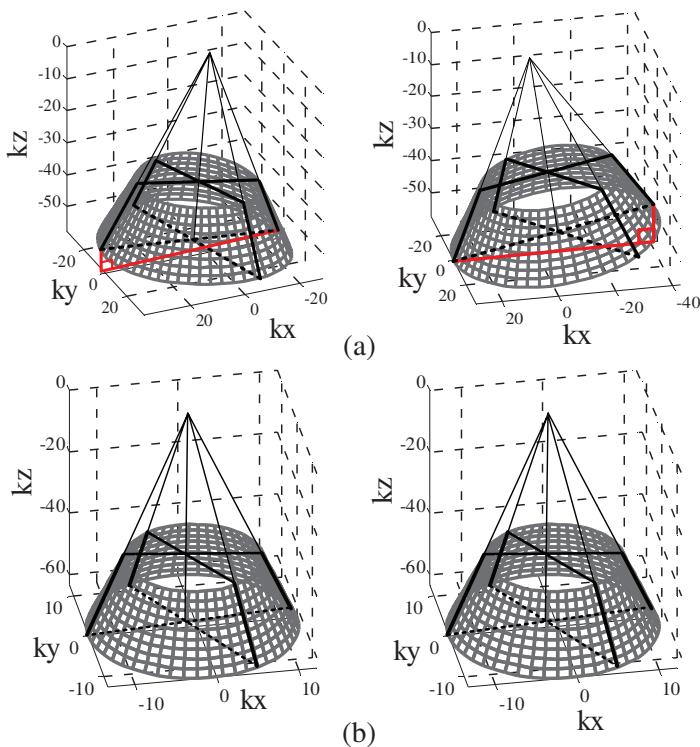


Figure 2. Data surfaces obtained in the spatial frequency space of scatterers with different positions. (a) Before resampling. (b) After resampling.

The time-domain simulator requires a reflectivity map as input, but the inverse image formation process requires an image as input to be as close as possible to a real system. It is useful to mention that the reflectivity map can be considered as an ideal image without band limiting or frequency support [8]. The reflectivity map can be converted to image by using the following operation:

$$I(k_x, k_y, k_z) = \Gamma(k_x, k_y, k_z)F_{\text{sup}}(k_x, k_y, k_z) \tag{9}$$

where $\Gamma(k_x, k_y, k_z)$ is the 3-D FT of the reflectivity map, and $F_{\text{sup}}(k_x, k_y, k_z)$ is given by

$$F_{\text{sup}}(k_x, k_y, k_z) = \begin{cases} 1, & \text{if } [k_x, k_y, k_z] \in \psi(k_x, k_y, k_z) \\ 0, & \text{otherwise} \end{cases} \quad (10)$$

An equivalent process is to convolve the reflectivity map in three dimensions with the processed image using 3-D FT. However, when assuming spherical wavefronts, PSFs in the processed image are spatially variant according to the discussion above. Thus, it is unable to realize the process efficiently. In [8], the reflectivity map was convolved with a reference point (in the middle of the scene). In [10], a large f_{PRF} (larger than the total Doppler bandwidth of the whole scenario) was used firstly. Then, the redundant synthetic time was truncated in the slow time domain. The requirement of computational complexity is fulfilled by the above two methods while the spatial variance of points in image is not fully achieved.

3. RAW DATA SIMULATION

3.1. Theory of the Algorithm

Traditional PFA applies PST with the assumption of planar wavefronts around a central reference point in the imaged scene [16, 17]. However, the presence of range curvature phase error limits effective scene size. Range curvature phase error is a spatially variant effect and increases with the distance between target and scene center. It is worth noticing that with the assumption of planar wavefronts, the frequency support is invariant for all points in the extended 3-D image, so that the operation in Equation (9) could be realized easily and efficiently. We apply the assumption of planar wavefronts in the first step so as to use FFT for efficiency. Then the conversion of planar wavefronts to spherical wavefronts is realized by a 1-D resampling operation.

Figure 3 is the sketch map of range 1-D resampling. Scatterers distribute on different spherical surfaces R_1, R_2, \dots, R_N . At a given R_i , the contour of a constant range ρ is a circle lies in a plane orthogonal to the SAR position vector. Let r_i be the perpendicular distance from the origin to such a plane for a given SAR location, then

$$r_i = R_i \cos \beta = \frac{r_S^2 + R_i^2 - \rho^2}{2r_S} \quad (11)$$

Let $E(r_i, \mathbf{r}_S)$ be the range compressed SAR raw data with the

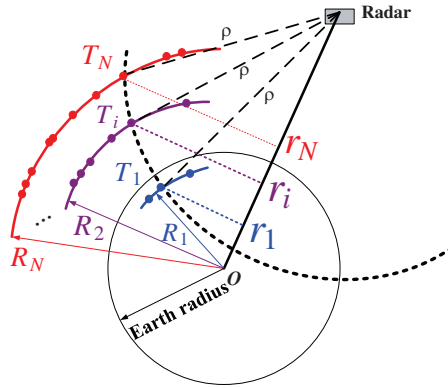


Figure 3. Sketch map of range resampling.

assumption of planar wavefronts. After projecting ρ to r_i , we can get

$$\begin{aligned}
 E(r_i, \mathbf{r}_S) &= E(\rho, \mathbf{r}_S) \cdot \exp \{j(k_c \rho - k'_c r)\} \\
 &= \iiint \sigma(x_T, y_T, z_T) q_r(r - r_P) \exp \{-jk'_c r_P\} dx_T dy_T dz_T \quad (12)
 \end{aligned}$$

where k' is the wavenumber of $E(r_i, \mathbf{r}_S)$ and

$$\begin{aligned}
 \gamma_{res} &= \left| \frac{dr}{d\rho} \Big|_{r=r_{mid}} \right| = -\frac{a_S}{\sqrt{a_S^2 + r_T^2 - 2a_S r_{mid}}}, \quad k'_c = -k_c / \gamma_{res} \\
 B' &\approx B / \gamma_{res}, \quad q(r - r_P) \approx \text{sinc} \left(\frac{2B'}{c} (r - r_P) \right) \quad (13)
 \end{aligned}$$

Via range FFT,

$$\begin{aligned}
 E(k', \mathbf{r}_S) &\approx \text{rect} \left(\frac{f'}{B'} \right) \iiint \sigma(x_T, y_T, z_T) \\
 &\quad \times g_{\mathbf{r}_S}^*(f', x_T, y_T, z_T) dx_T dy_T dz_T \quad (14)
 \end{aligned}$$

$g_{\mathbf{r}_S}^*(f', x_T, y_T, z_T)$ is the SAR imaging system's shift-varying impulse response function after resampling:

$$g_{\mathbf{r}_S}^*(f', x_T, y_T, z_T) = \exp \{-jk' \cdot r_P\} \quad (15)$$

From Equation (7), we can get

$$\begin{aligned}
 r &= (\mathbf{r}_T \cdot \mathbf{r}_S) / |\mathbf{r}_S| \\
 &= x_T \sin \alpha_S \cos \theta_S + y_T \sin \alpha_S \sin \theta_S + z_T \cos \alpha_S \quad (16)
 \end{aligned}$$

Let (k_x, k_y, k_z) be the instantaneous wavenumber and they relate to (k', α_S, θ_S) via

$$\begin{cases} k_x = k' \sin \alpha_s \cos \theta_S \\ k_y = k' \sin \alpha_s \sin \theta_S \\ k_z = k' \cos \alpha_s \end{cases} \quad (17)$$

From Equation (15), $g_{\mathbf{r}_S}^*(f', x_T, y_T, z_T)$ could be expressed as

$$g_{\mathbf{r}_S}^*(f', x_T, y_T, z_T) = \exp\{-j(k_x x_T + k_y y_T + k_z z_T)\} \quad (18)$$

Via interpolation, the polar samples of $E(r_i, \mathbf{r}_S)$ could be converted to 3-D frequency format:

$$\begin{aligned} E(k_x, k_y, k_z, \mathbf{r}_S) &= F'_{\text{sup}}(k_x, k_y, k_z) \iiint \sigma(x_T, y_T, z_T) \\ &\quad \times \exp\{-j(k_x x_T + k_y y_T + k_z z_T)\} dx_T dy_T dz_T \\ &= F'_{\text{sup}}(k_x, k_y, k_z) \Gamma(k_x, k_y, k_z) \end{aligned} \quad (19)$$

where $F'_{\text{sup}}(k_x, k_y, k_z)$ is calculated by Equation (17), and the corresponding frequency support $\psi'(k_x, k_y, k_z)$ is determined by k' and the sensor trajectories. Figure 2(b) shows the 3-D data surface in the spatial frequency space after resampling. It is obvious that the frequency support is invariant with target position.

3.2. Implementation of the Simulation

Figure 4 shows the major processing steps. N_r and N_a represent the number of fast-time samples and the number of slow-time samples, respectively. N_T^3 is the image size and M_{ker} is the 1-D interpolator length.

Step 1) Convert the reflectivity map to image. Assuming planar wavefronts and using a time-domain simulator, raw data of a single point in the scene with arbitrary position is generated and then processed by the back-projection (BP) algorithm to obtain $F'_{\text{sup}}(k_x, k_y, k_z)$. Assume that all scatterers distribute in N different spherical surfaces. The 3-D reflectivity pattern is divided into N groups according to surfaces. Convolve every group of 3-D reflectivity map with the processed point using 3-D FFT to obtain $E(k_x, k_y, k_z, \mathbf{r}_S)$. The computational complexity is $O(N(N_T^3 \log_2(N_T) + N_T^3))$.

Step 2) Convert every Cartesian format data $E(k_x, k_y, k_z, \mathbf{r}_S)$ to polar format data $E(k', \mathbf{r}_S)$ via a 3-D interpolation. For every θ , $k' \in [k'_c - B'/2, k'_c + B'/2]$. According to Equation (13), k'_c and B' vary with slow-time. Thus, to obtain final raw signal with fixed carrier frequency k_c and bandwidth B , let $k'_c = k_c/\beta$, $B' = B/\beta$ when

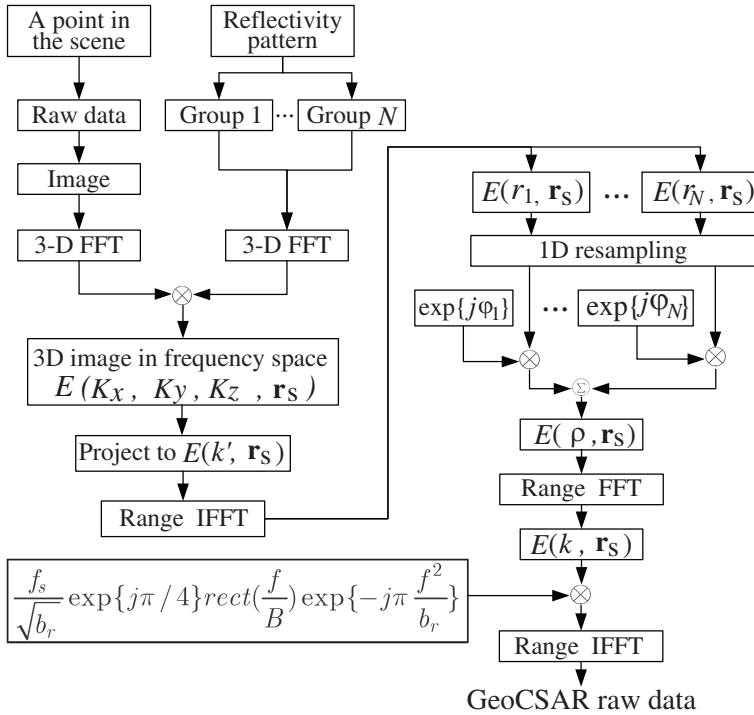


Figure 4. Flow diagram of the simulation procedure.

interpolate (k_x, k_y, k_z) to (k', θ) . The computational complexity is $O(M_{ker}N_aN_rN)$.

Step 3) Range IFFT to transform $E(k', \mathbf{r}_S)$ to $E(r_i, \mathbf{r}_S)$. The computational complexity of this step is $O(N_aN_r \log N_rN)$.

Step 4) Map r_i to ρ via 1-D resampling. Resampling process is operated for every $E(r_i, \mathbf{r}_S)$ according to Equation (11). Multiply $\exp\{j\varphi_i\}$ to the resampled signal, where $\varphi_i = k'_c r_i - k_c \rho$. Then, all the outputs are added to achieve $E(\rho, \mathbf{r}_S)$. The computational complexity is $O(M_{ker}N_aN_rN)$.

Step 5) Range FFT to transform $E(\rho, \mathbf{r}_S)$ to $E(k, \mathbf{r}_S)$. The phase of the transmitted chirp is multiplied. Then, a range IFFT is done to generate the GeoCSAR raw data. The computational complexity is $O(N_aN_r \log N_r + N_aN_r)$.

4. SIMULATION RESULTS

First, raw data of discrete targets are simulated both by the proposed method and time-domain method. Results are compared both in

amplitude and in phase. Second, a real SAR image is utilized as a reflectivity pattern.

The main system parameters are listed in Table 1. The locations of six discrete scattering targets are shown in Table 2. Target No. 1 is on the scene center. Target Nos. 2–3 are near target No. 1. Target Nos. 5–6 are near the border of the scene.

Figure 5 shows the simulated raw data by the proposed method and time-domain method. The disturbance added on orbit is exaggerated to show the feasibility of the proposed method in generating raw data for arbitrary trajectories. Figure 6 shows the amplitudes of the range and azimuth signals at some range and azimuth lines, respectively. It can be seen that the amplitudes match ideal amplitudes quite well. Both range amplitude and azimuth amplitude vary with ideal amplitudes slightly due to: (1) the variation of amplitude function $q(r - r_P)$ in range direction introduced by the non-linear 1-D resampling process; (2) the Fresnel undulation caused by adding a chirp signal in the frequency domain; (3) the big coupling between the range and azimuth. The differences of the raw data phase with respect to the time-domain simulated data are shown in Figure 7. The absolute value of the phase error is always less than $\pi/60$, thus leading to negligible effects.

The detailed target No. 5 and No. 6 are shown in Figure 8 and Figure 9. The GeoCSAR 2-D resolution function is approximated as Bessel function. From Figure 8 and Figure 9, the sidelobes of Bessel functions of target No. 5 and No. 6 is asymmetric, which is due to the inclination of the PSFs. It can be seen that the spatial variance of targets is precisely performed.

Table 1. Simulation parameters.

Parameter	Value	Parameter	Value
Carrier Frequency	1.3 GHz	Sampling Rate	360 MHz
$d\theta$	1.2°	Bandwidth	300 MHz
Orbit inclination	0.1 rad	Orbit eccentricity	0.05

Table 2. Locations of the discrete points.

Tar. No.	Location (x, y, z) m	Tar. No.	Location (x, y, z) m
1	(0, 0, 0)	4	(0, -100, 0)
2	(0, 0, 20)	5	(0, 10000, 1000)
3	(110, 110, 0)	6	(-10000, -10000, 1000)

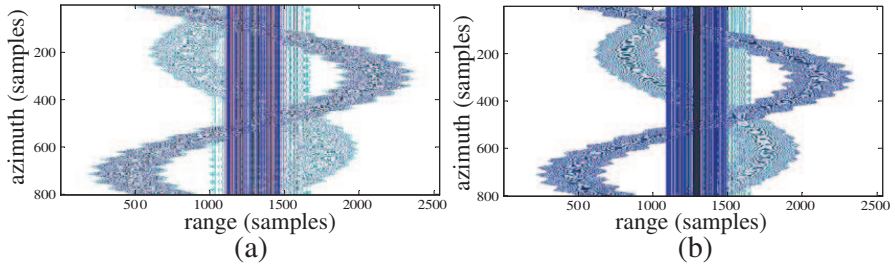


Figure 5. Simulated SAR raw data of target No. 1–No. 4. (a) The proposed method. (b) Time-domain method.

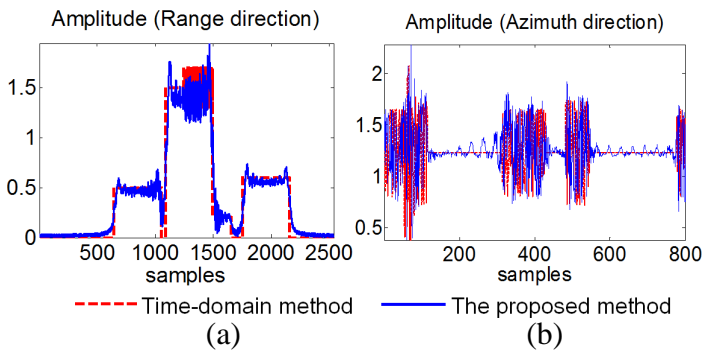


Figure 6. Amplitude of the simulated signal in the time domain. (a) Range direction. (b) Azimuth direction of Target No. 1.

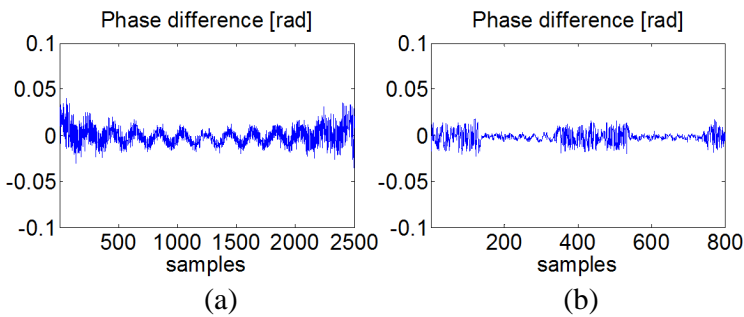


Figure 7. Phase errors. (a) Range direction. (b) Azimuth direction.

The quality metric of imaging results from the raw data generated by time-domain method and the proposed method are listed in Table 3, including 3 dB impulse response width (IRW), peak sidelobe ratio (PSLR) and integrated sidelobe ratio (ISLR). From Table 3, it can be

concluded that the proposed method has a comparable performance to time-domain method, but works more efficiently.

In order to further demonstrate the efficiency of the proposed method, a real high resolution CSAR image after processing 360° of the circular aperture [11] is utilized as the reflectivity pattern (see Figure 10(a)). The image size is 8192×8192 pixels. Assume $N = 1$ due to the fact that the reflectivity pattern is a 2-D one. The imaging result is shown in Figure 10(b). The rectangular region marked by the red rectangle in Figure 10(a) and Figure 10(b) is displayed separately in Figure 11. On the assumption that all of the targets in the reflectivity pattern are isotropic, the simulated scene shows obvious high sidelobes

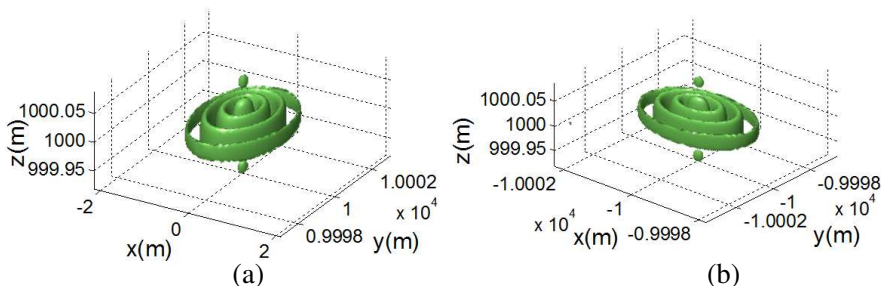


Figure 8. Expanded image of the point target. The displayed dynamic range is 20 dB. (a) Target No. 5. (b) Target No. 6.

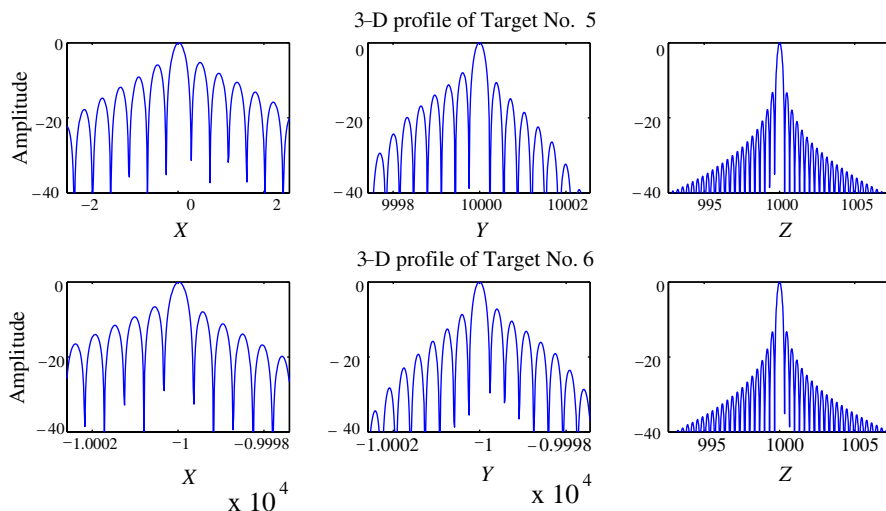


Figure 9. 3-D profile of Target No. 5 and Target No. 6.

Table 3. Image quality parameters.

Tar. No.	Axis	The proposed method			Time-domain method		
		IRW (m)	PSLR	ISLR	IRW (m)	PSLR	ISLR
5	X	0.3395	-8.0101	-3.6270	0.3398	-8.0205	-3.6755
	Y	0.3411	-8.0033	-3.6731	0.3469	-8.0031	-3.7004
	Z	0.47	-13.0660	-9.6461	0.4602	-13.0785	-9.6829
6	X	0.3368	-8.0261	-3.6598	0.3418	-8.0247	-3.6438
	Y	0.3423	-8.0184	-3.6820	0.3413	-8.0176	-3.7051
	Z	0.47	-13.0655	-9.7288	0.4705	-13.0710	-9.6912

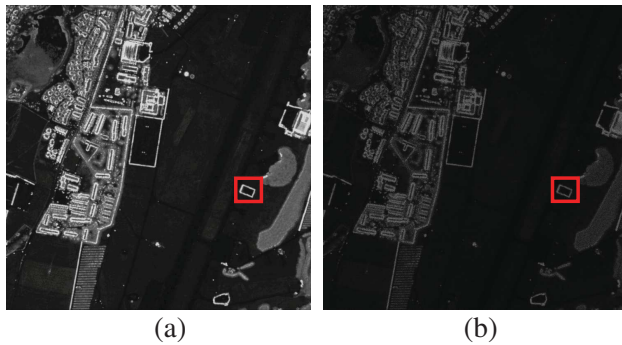


Figure 10. (a) Reflectivity pattern of the scene. (b) Simulated scene.

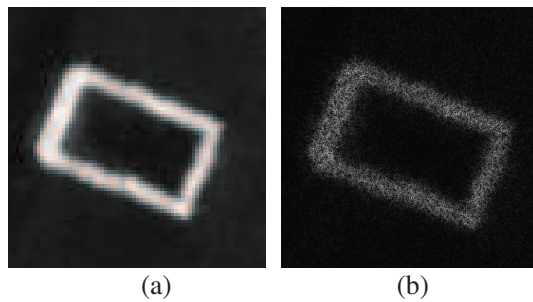


Figure 11. Zoom out figure of the marked area in Figure 10.

due to the GeoCSAR configuration. Figure 12 gives the processed image with wrong reference heights of 4 m and 8 m. The target appears focused at its true height and as the height is increased or decreased the defocusing phenomena appears. The tomographic results show that by using the proposed method, the achieved raw data could be used for 3-

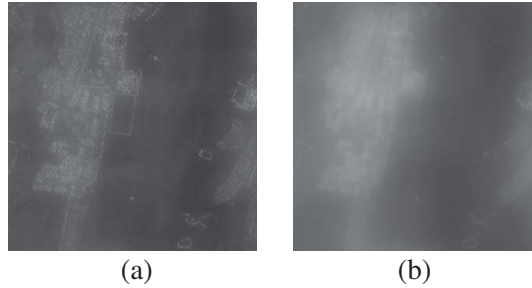


Figure 12. Processed image with wrong reference heights of (a) 4 m and (b) 8 m.

Table 4. Computational complexity comparison.

Method	Computational complexity	Applicability
Time-domain method	$O(N_T^3 N_a N_r)$	Arbitrary aperture
Conventional 2-D frequency method	$O(N_a N_r + N_a N_r (\log N_a + \log N_r))$	Ideal linear aperture only
The proposed method	$O(N M_{\text{ker}} N_a^2 N_r + N N_a N_r (\log N_a + \log N_r))$	Arbitrary aperture

D reconstruction of targets in GeoCSAR configuration. The raw data simulation cost about 27 minutes on an Intel Core2 E7200 2.53 GHz PC. It would require several weeks if using time-domain simulator on the same PC.

Table 4 gives the comparison of existing methods. From Table 4, it is obvious that when the size of scene increases, the proposed method has more advantage in computational complexity.

5. CONCLUSIONS

An efficient GeoCSAR raw data simulator has been presented, which is an inverse process of the improved PFA. The method enables the simulator to use Fast Fourier transform for efficiency and employs a conversion of planar wavefronts to spherical wavefronts 1-D resampling operation to generate raw data for non-ideal sensor trajectories precisely. Validated numerically, the method has a close accuracy compared with time-domain simulator but performs more efficiently.

ACKNOWLEDGMENT

This work was supported in part by the National Science Fund for Distinguished Young Scholars under Grant 60725103, and the National Natural Science Foundation of China under Grant 60890070.

REFERENCES

1. Tomiyasu, K. and J. Pacelli, "Synthetic aperture radar imaging from an inclined geosynchronous orbit," *IEEE Trans. Geosci. Remote Sens.*, Vol. 21, No. 3, 324–329, 1983.
2. Long, T., X. Dong, C. Hu, and T. Zeng, "A new method of zero-doppler centroid control in GEOSAR," *IEEE Geosci. Remote Sens. Lett.*, Vol. 8, No. 3, 512–516, 2011.
3. Liu, Q., W. Hong, W.-X. Tan, Y. Lin, Y.-P. Wang, and Y.-R. Wu, "An improved polar format algorithm with performance analysis for geosynchronous circular SAR 2D imaging," *Progress In Electromagnetics Research*, Vol. 119, 155–170, 2011.
4. Zhao, Y.-W., M. Zhang, and H. Chen, "An efficient ocean SAR raw signal simulation by employing fast fourier transform," *Journal of Electromagnetic Waves and Applications*, Vol. 24, No. 16, 2273–2284, 2010.
5. Koo, V. C., C. S. Lim, and Y. K. Chan, "iSim — An integrated SAR product simulator for system designers and researchers," *Journal of Electromagnetic Waves and Applications*, Vol. 21, No. 3, 313–328, 2007.
6. Mori, A. and F. De Vita, "A time-domain raw signal simulator for interferometric SAR," *IEEE Trans. Geosci. Remote Sens.*, Vol. 42, No. 9, 1811–1817, 2004.
7. Smolarczyk, M., "Radar signal simulator for SAR algorithms test," *Proc. IRS*, 509–515, Dresden, Germany, 2003.
8. Khwaja, A. S., L. Ferro-Famil, and E. Pottier, "Efficient SAR raw data generation for anisotropic urban scenes based on inverse processing," *IEEE Geosci. Remote Sens. Lett.*, Vol. 6, No. 4, 757–761, 2009.
9. Qiu, X.-L., D.-H. Hu, L.-J. Zhou, and C.-B. Ding, "A bistatic SAR raw data simulator based on inverse ω -k algorithm," *IEEE Trans. Geosci. Remote Sens.*, Vol. 48, No. 3, 1540–1547, 2010.
10. Cimmino, S., G. Franceschetti, and A. Iodice, "Efficient spotlight SAR raw signal simulation of extended scenes," *IEEE Trans. Geosci. Remote Sens.*, Vol. 41, No. 10, 2329–2337, 2003.

11. Ponce, O., P. Prats, M. Rodriguez-Cassola, R. Scheiber, and A. Reigber, "Processing of circular SAR trajectories with fast factorized back-projection," *Proc. IGARSS*, 3692–3695, Vancouver, Canada, 2011.
12. Tan, W.-X., W. Hong, Y.-P. Wang, and Y.-R. Wu, "A novel spherical-wave three-dimensional imaging algorithm for microwave cylindrical scanning geometries," *Progress In Electromagnetics Research*, Vol. 111, 43–70, 2011.
13. Yu, L. and Y. Zhang, "A 3D target imaging algorithm based on two-pass circular SAR observations," *Progress In Electromagnetics Research*, Vol. 122, 341–360, 2012.
14. Zhang, M., Y.-W. Zhao, H. Chen, and W.-Q. Jiang, "SAR imaging simulation for composite model of ship on dynamic ocean scene," *Progress In Electromagnetics Research*, Vol. 113, 395–412, 2011.
15. Chang, Y.-L., C.-Y. Chiang, and K.-S. Chen, "SAR image simulation with application to target recognition," *Progress In Electromagnetics Research*, Vol. 119, 35–57, 2011.
16. Sun, J.-P., S.-Y. Mao, G.-H. Wang, and W. Hong, "Extended exact transfer function algorithm for bistatic SAR of translational invariant case," *Progress In Electromagnetics Research*, Vol. 99, 89–108, 2009.
17. Nie, X., D.-Y. Zhu, and Z.-D. Zhu, "Application of synthetic bandwidth approach in SAR polar format algorithm using the deramp technique," *Progress In Electromagnetics Research*, Vol. 80, 447–460, 2008.
18. Mao, X.-H., D.-Y. Zhu, L. Ding, and Z.-D. Zhu, "Comparative study of RMA and PFA on their responses to moving target," *Progress In Electromagnetics Research*, Vol. 110, 103–124, 2010.